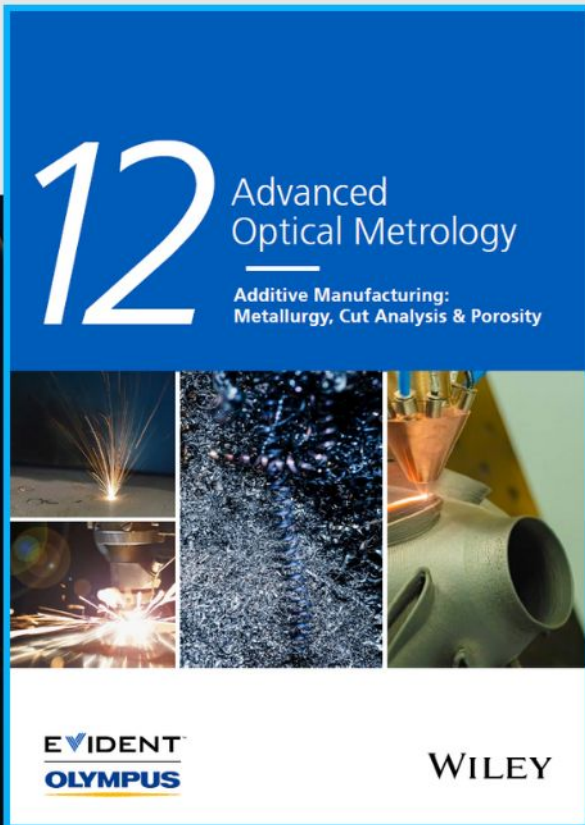




Additive Manufacturing: Metallurgy, Cut Analysis & Porosity



The latest eBook from
Advanced Optical Metrology.
Download for free.

In industry, sector after sector is moving away from conventional production methods to additive manufacturing, a technology that has been recommended for substantial research investment.

Download the latest eBook to read about the applications, trends, opportunities, and challenges around this process, and how it has been adapted to different industrial sectors.

EVIDENT™
OLYMPUS

WILEY

Mechanisms of Interface Cleaning in Heterostructures Made from Polymer-Contaminated Graphene

Zhujun Huang, Edoardo Cuniberto, Suji Park, Kim Kisslinger, Qin Wu, Takashi Taniguchi, Kenji Watanabe, Kevin G. Yager, and Davood Shahrjerdi*

Heterostructures obtained from layered assembly of 2D materials such as graphene and hexagonal boron nitride have potential in the development of new electronic devices. Whereas various materials techniques can now produce macroscopic scale graphene, the construction of similar size heterostructures with atomically clean interfaces is still unrealized. A primary barrier has been the inability to remove polymeric residues from the interfaces that arise between layers when fabricating heterostructures. Here, the interface cleaning problem of polymer-contaminated heterostructures is experimentally studied from an energy viewpoint. With this approach, it is established that the interface cleaning mechanism involves a combination of thermally activated polymer residue mobilization and their mechanical actuation. This framework allows a systematic approach for fabricating record large-area clean heterostructures from polymer-contaminated graphene. These heterostructures provide state-of-the-art electronic performance. This study opens new strategies for the scalable production of layered materials heterostructures.

1. Introduction

The layered assembly of 2D materials into van der Waals (vdW) heterostructures has enabled numerous fundamental and applied research.^[1–9] Almost all studies require clean heterostructures that contain minimal interfacial and material disorder, as their presence diminishes the quality of the resulting 2D electronic systems.^[10–14] While considerable technical advances in recent years have enabled the construction of high-quality heterostructures, they have a small size (typically a few 10s of μm), and their production yield is low. Overcoming these limitations is a critical need for advancing these heterostructures toward technological applications.

The construction of clean heterostructures currently involves two general best practices. The first is to extract low-defect 2D layers by disassembling the bulk crystals of those materials. The other is to avoid the exposure of resulting 2D layers to contaminants (e.g., polymers, solvents) during the entire layer assembly and device fabrication. Following these guidelines, heterostructures are commonly made by employing a combination of the conventional Scotch-tape exfoliation onto clean SiO_2 substrates and the encapsulation of 2D layers in hexagonal boron nitride (hBN)—also known as the dry transfer technique.^[14] Electronic devices prepared using this technique currently provide state-of-the-art performance.^[14–16]

However, the poor outcome of the conventional exfoliation method, in terms of the size and yield of exfoliated 2D layers, limits the dimensions and the fabrication throughput of clean heterostructures. To overcome these shortcomings, modified exfoliation methods have been developed for disassembling layered crystals.^[17–27] Polymer films are vital to the implementation of most of these methods. For example, we have previously shown that a simple modification of the exfoliation substrate with a thin layer of polymer (polyvinyl alcohol, PVA) can significantly improve the size and yield of monolayer graphene.^[25] Also, significant progress has been made in preparing low-defect 2D layers using scalable material growth techniques (e.g., chemical vapor deposition, CVD).^[26,27] Polymers (e.g., polymethyl methacrylate, PMMA) are routinely used as the backing layer for releasing the CVD films from the metallic growth substrate.^[28–30] The continued reliance on polymer films indicates


Z. Huang, E. Cuniberto, D. Shahrjerdi
Electrical and Computer Engineering
New York University
Brooklyn, NY 11201, USA
E-mail: davood@nyu.edu

S. Park, K. Kisslinger, Q. Wu, K. G. Yager
Center for Functional Nanomaterials
Brookhaven National Laboratory
Upton, NY 11973, USA

T. Taniguchi
International Center for Materials Nanoarchitectonics
National Institute of Materials Science
1-1 Namiki Tsukuba, Ibaraki 305-0044, Japan

K. Watanabe
Research Center for Functional Materials
National Institute of Materials Science
1-1 Namiki Tsukuba, Ibaraki 305-0044, Japan

D. Shahrjerdi
Center for Quantum Phenomena
Physics Department
New York University
New York, NY 10003, USA

 The ORCID identification number(s) for the author(s) of this article can be found under <https://doi.org/10.1002/sml.202201248>.

DOI: 10.1002/sml.202201248

the prospects of polymer-based techniques for preparing and handling of 2D layers in technological applications.

The dimension of graphene layers prepared using these large-area techniques has reached macroscopic scales (>100 μm , and even up to wafer scales). However, the resulting graphene layers are inevitably contaminated with polymer residues during preparation, resulting in numerous interfacial imperfections (also referred to as blisters) when using them for constructing heterostructures.^[16,20,22,28] Hence, the potential of these large-area techniques for technological applications remains largely unrealized due to the inability to produce macroscopic-scale multilayer heterostructures with atomically clean interfaces.

It is currently thought that thermal actuation (i.e., applying heat to activate blisters) is the primary mechanism for cleaning interfaces in vdW heterostructures.^[16,28] A recent study by Purdie et al. indicates that an actuation temperature in the range of 150 to 250 $^{\circ}\text{C}$ is optimal for achieving blister-free heterostructures.^[16] The lower bound of 150 $^{\circ}\text{C}$ matches the glass transition temperature of the elastomeric stamp and the upper bound of 250 $^{\circ}\text{C}$ presents the temperature at which surface energies (between graphene and SiO_2) are maximal. This study showed experimentally that a temperature of 180 $^{\circ}\text{C}$ is sufficient for removing blisters from an entire dimension of large heterostructures (up to 5000 μm^2) made from conventionally exfoliated graphene. However, the application of this thermal actuation process on exfoliated graphene contaminated with PMMA and organic solvents has not reproduced a similar outcome. Only small regions of those heterostructures (maximum area of $\approx 600 \mu\text{m}^2$) appeared blister-free, even when applying temperatures as high as 250 $^{\circ}\text{C}$.^[16] The dimensions of blister-free regions are even smaller when this process was applied to heterostructures made from CVD graphene, where graphene was transferred from the growth substrate with the aid of PMMA backing layer.^[28] The underlying reasons behind the observed incomplete cleaning of PMMA-contaminated graphene heterostructures are currently unknown. These observations, however, indicate that the interface cleaning of polymer-contaminated graphene involves more complex mechanisms than originally thought.

Here, we study this problem by presenting a simplified picture of the interface cleaning process in heterostructures made from polymer-contaminated graphene. Briefly, we hypothesize that the mobilization of polymer residues and their mechanical actuation (i.e., through applying elastic energy by the stamp) are the required processes that underlie the interface cleaning of such heterostructures. This simplified picture sets up a systematic framework for analyzing this problem from an energy viewpoint. This analysis suggests that non-bonding interactions of polymer with 2D layers (including those containing structural defects) are essential for mobilizing the polymer. Our density functional theory (DFT) calculations indicate PVA molecules have weak non-bonding interactions with pristine graphene. Also, they are less likely to bond covalently to defective graphene. Guided by these findings, therefore we perform interface cleaning experiments using PVA-contaminated graphene.

Our experiments revealed a cleaning temperature threshold of 230 $^{\circ}\text{C}$ for removing the interfacial PVA residues. We

observe negligible interface cleaning below this threshold temperature. Hence, contrary to common belief, thermal actuation alone is insufficient for cleaning polymer-contaminated interfaces. Another mechanism must drive the thermal activation of polymer residues. Interestingly, the 230 $^{\circ}\text{C}$ threshold coincides with the temperature at which PVA molecules are known to undergo marked structural relaxation.^[31] This reduces the surface energy of PVA residues, thus facilitating their mobilization.^[32–34] Last, our systematic experiments reveal insights into the role of mechanical actuation in cleaning polymer-contaminated vdW interfaces. We show how the global and local deformations of the elastomeric stamp influence the removal of thermally activated mobilized polymer residues.

Our study here establishes that the interface cleaning process of heterostructures made from polymer-contaminated 2D layers involves a more complex mechanism than a simple thermal actuation. A combination of non-bonding interactions of polymer with graphene, thermally activated mobilization of polymer residues, and mechanical actuation is essential for fabricating heterostructures with atomically clean interfaces when employing polymer contaminated graphene. By using PVA-contaminated exfoliated graphene as the model system, we demonstrate a systematic fabrication of clean hBN-encapsulated graphene (BGB) heterostructures with record large dimensions up to 7500 μm^2 . These heterostructures provide state-of-the-art electronic performance.

2. Results

2.1. Construction of BGB Heterostructures

We designed our experiments around graphene contaminated with PVA and subsequently encapsulated in hBN. **Figure 1** illustrates the key steps of our experiments (see Experimental Section for details). The experiments started with the preparation of monolayer graphene using a modified mechanical exfoliation method, referred to as PVA-assisted graphene exfoliation (PAGE, Figure 1a).^[25] This method consistently produces large monolayer graphene with dimensions exceeding 100 μm . Another advantage of PAGE is that it exposes graphene to only water and PVA, thus limiting the contamination sources. Figure 1d shows the optical image of monolayer graphene produced by PAGE (see Figure S1, Supporting Information, for additional examples). Next, monolayer graphene was released by locally dissolving the PVA film underneath it and attached to an elastomeric stamp carrying a top hBN flake (t-hBN), as illustrated in Figure 1b,1e.

The next is the encapsulation step, where we encapsulate monolayer graphene in between two hBN flakes, resulting in BGB heterostructures. This step is performed by heat-assisted lamination of the t-hBN/graphene heterobilayer onto a bottom hBN (b-hBN) flake (Figure 1c). In our experiments, the elastomeric stamps had a hemispherical shape and were covered with poly (bisphenol A carbonate) (PC) which acted as the phase-change elastomeric layer (see Experimental Section). In all encapsulations, the substrate temperature was set well above the glass transition temperature of PC (150 $^{\circ}\text{C}$) to ensure its phase transition. Once the stamp touches the substrate, it

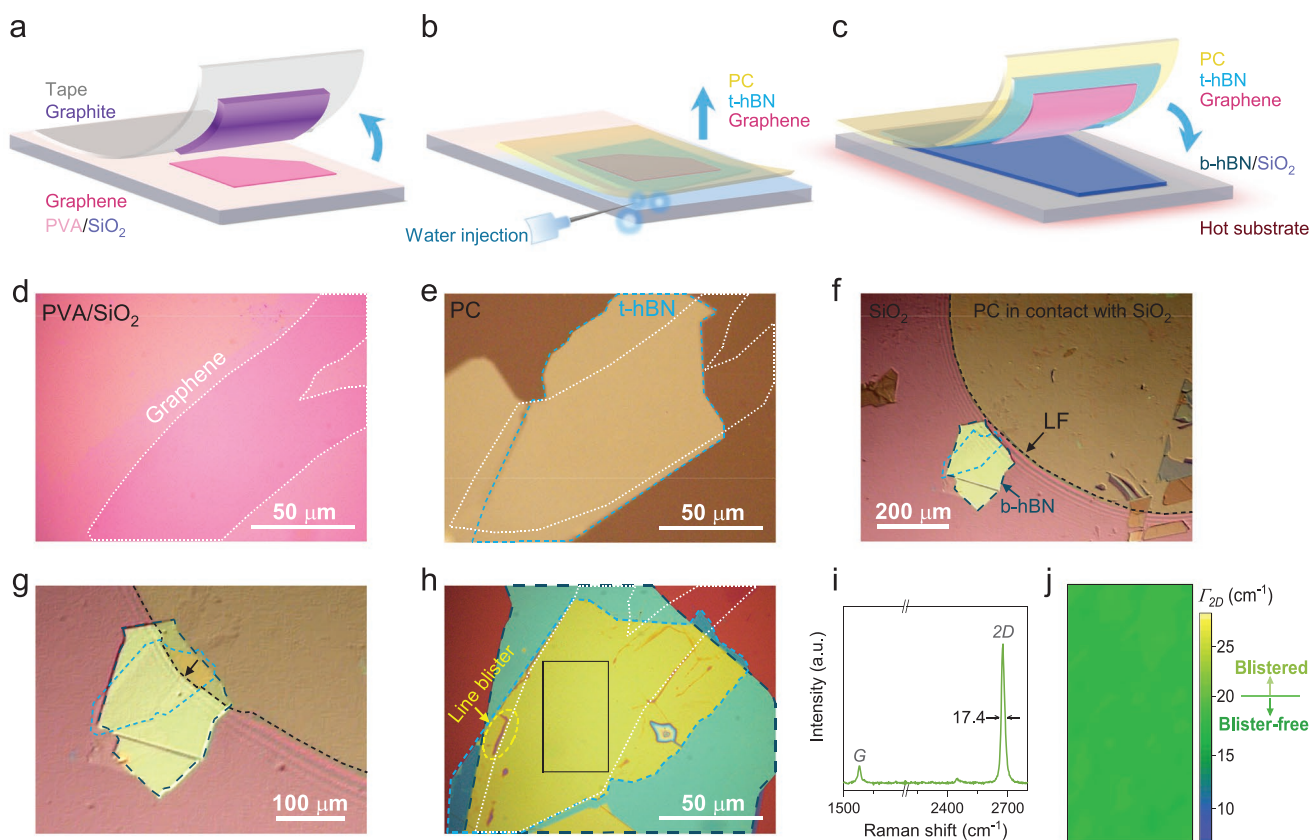


Figure 1. Construction of BGB heterostructures. Schematic illustrations of a) PAGE process, b) formation of t-hBN/graphene heterobilayer, and c) encapsulation process. d) Optical image of a large ($> 8000 \mu\text{m}^2$) monolayer graphene on PVA/SiO₂ substrate. e) Optical image of the heterobilayer made from the same graphene flake. Optical images captured during the encapsulation process showing LF f) after landing the stamp on the substrate, and g) on the b-hBN. Arrows in (f) and (g) indicate the direction of the LF propagation. h) Optical image of the final BGB heterostructure, showing complete interface cleaning across the entire heterostructure. Interfacial contaminants were pushed to the borders of the heterostructure. A representative line blister is marked with a yellow dashed circle. The area of the blister-free region here is $\approx 6000 \mu\text{m}^2$. i) A representative Raman spectrum of graphene obtained from the BGB heterostructure. j) Spatial Γ_{2D} map of the region marked with a solid rectangle in panel (h), confirming the absence of blisters.

results in an initial circular lamination front (LF) (Figure 1f). The LF advances laterally as the stamp is lowered (i.e., pressed down) mechanically in the vertical direction (Figure 1g) until the BGB stack is fully formed.

The accumulation of contaminants during the encapsulation step is known to cause interfacial imperfections (i.e., blisters).^[35–38] Past research has shown that water and gaseous blisters—generally forming across heterostructures made using the dry transfer technique—are easy to clean simply by using thermal actuation.^[16,39] In contrast, blisters formed due to polymeric residues (e.g., upon exposure to PMMA or PVA) appear to be stagnant, preventing the cleaning across an entire dimension of heterostructures when employing a similar thermal actuation process. As a result, interface cleaning of polymer-exposed graphene has been limited to a small area of the heterostructure.^[16,28] A complete interface cleaning over the entire dimension of polymer-contaminated BGB heterostructures is yet to be realized. A barrier to progress is the incomplete understanding of the mechanisms for interface cleaning of such heterostructures.

We overcome this challenge by introducing a systematic framework that establishes the mechanisms for removing

polymer residues from vdW interfaces across graphene heterostructures. We set up this framework with the aid of a simplified picture of the interface cleaning, as shown in Figure 2a. This approach allows the study of this problem from an energy viewpoint. We posit that the interface cleaning across the entire heterostructure is attainable by simultaneously satisfying two requirements. The first requirement is to mobilize polymeric contaminants at LF. We hypothesize that mobilization requires weak non-bonding interactions between the polymer molecules and 2D layers and decreasing the free surface energy of the polymer. Polymer science studies suggest that the latter could be achieved by applying sufficient thermal energy to the polymer (which we call thermal activation for mobilizing polymer).^[32–34]

The second requirement is to push the mobilized contaminants away from LF. We hypothesize that the elastic deformation of the stamp must generate a sufficiently high driving force to overcome the energy of the residues at LF. A combination of the vertical pressure exerted by the stamp and the melting of the PC elastomer induce the driving force. Satisfying these two requirements will result in the propagation of residues across the heterostructure.

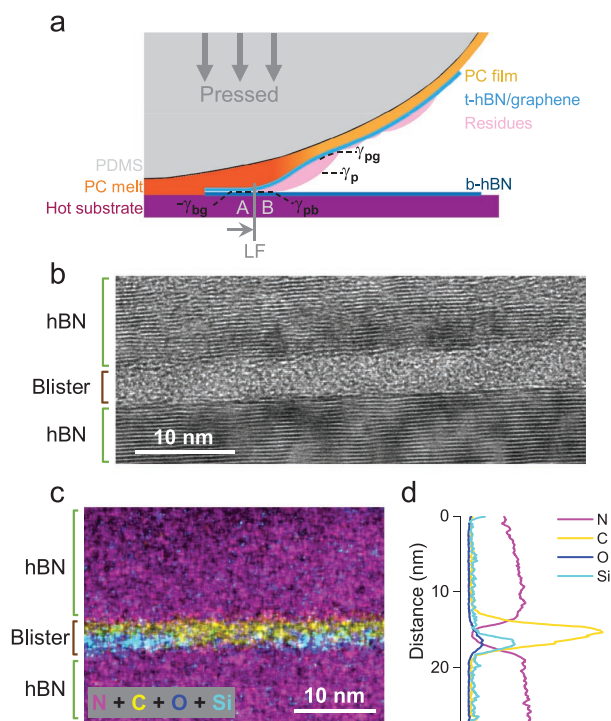


Figure 2. Simplified framework of interface cleaning. a) Side-view schematic illustrating the physical processes involved in removing the polymeric residues during encapsulation. As the stamp touches the substrate, PC softens and becomes a polymer melt. The PC film regions farther from the substrate remain at a lower temperature and thus stiffer. The stamp is lowered mechanically in the vertical direction, causing LF to advance laterally (LF propagation direction is marked by an arrow). As LF advances, the interface cleaning occurs if a new interface is formed between graphene and b-hBN behind LF (Region A) and simultaneously the contaminants are pushed to the front of LF (Region B) by the stamp deformation. b) A representative cross-sectional HRTEM image obtained from the blistered heterostructure. c) Corresponding EDS map and (d) averaged line intensity profiles of different elements.

We set up a systematic framework to test the validity of the above hypotheses. Our findings, as we describe later, lead to a systematic approach for fabricating clean BGB heterostructures. We establish the experimental conditions to reproducibly achieve complete removal of polymer residues from the vdW interfaces across the entire dimension of the BGB heterostructures. An example heterostructure is shown in Figure 1h (see Figure S2, Supporting Information, for additional examples). The Raman signature of graphene also gives information about the quality of the interface.^[40,41] In Figure 1i, we show a representative Raman spectrum obtained from the graphene in Figure 1h. The narrow full width at half maximum of the graphene 2D peak (Γ_{2D}) indicates the cleanliness of the interface.^[16,41] The spatial map of Γ_{2D} in Figure 1j further confirms the cleanliness of the heterostructure.

The clean regions of the PVA-contaminated BGB heterostructures resulting from our approach are over 10 times larger than the previous champion PMMA-contaminated heterostructure reported in ref. [16]. As shown in Figure 1h, our method cleans vdW interfaces in the entirety of the graphene region, up the boundary of the heterostructure. Our study is the first

to demonstrate a complete polymer removal from the entire dimensions of BGB heterostructures. Further increase of the clean regions will be possible by employing larger hBN crystals.

2.2. Framework for Interface Cleaning of Polymer-Contaminated Heterostructures

Figure 2a conceptually illustrates our proposed simplified picture of the mechanisms behind removing interfacial polymer residues in vdW heterostructures. This conceptual representation allows us to study the interface cleaning process from an energy viewpoint. In this illustration, LF is advancing from left to right as the stamp is pressed down. The interface cleaning occurs if, as the LF advances, a new interface between graphene and b-hBN is formed behind LF (i.e., Region A) while contaminants are pushed to the front of LF (i.e., Region B). Specifically, the interface cleaning takes place if the elastic energy generated by the stamp (γ_{elastic}) exceeds the energy at LF (γ_{LF}). The larger this energy gap is, the higher the likelihood of interface cleaning.

The proposed simplified framework focuses our study here on the interface cleaning of the polymer-contaminated interface (i.e., the bottom interface). Specifically, the top surface of graphene in our experiments is not exposed to PVA, thus its interface with t-hBN can be considered similar to that of a conventionally exfoliated graphene with hBN. Based on the previous studies,^[16,28] we know that blisters in such interfaces are noticeably easier to remove (simply by employing thermal actuation) than those in polymer-contaminated interfaces. Therefore, we inferred that the polymer-contaminated interface is the main bottleneck in removing blisters across the entire dimension of heterostructures. Our controlled experiments on conventional and PVA-contaminated graphene heterostructures (see Figure S3, Supporting Information) further support the validity of this abstraction of the interface cleaning problem.

The energy at LF depends on the composition of the contaminants. Our experiments indicate that the contaminants are primarily polymeric residues (described in “composition of the interfacial contaminants”). With this knowledge and from the proposed framework in Figure 2a, the energy at LF has four components: the interfacial energy between the polymeric residue and graphene (γ_{pg}), the interfacial energy between the polymeric residue and b-hBN (γ_{pb}), the surface energy of the polymeric residue (γ_{p}), and the energy release due to the formation of the new interface between b-hBN and graphene (γ_{bg}). Therefore, we can write γ_{LF} as follows:

$$\gamma_{\text{LF}} = \gamma_{\text{pg}} + \gamma_{\text{pb}} + \gamma_{\text{p}} - \gamma_{\text{bg}} \quad (1)$$

where the minus sign in front of γ_{bg} is due to the release of energy as a result of the formation of a new interface. We will study how γ_{LF} can be reduced by analyzing the interfacial energies (γ_{pg} , γ_{pb}) and the surface energy of the polymeric residue (γ_{p}) in the subsequent sections (“polymer interfacial energies” and “polymer surface energy”).

In our framework, the elastic energy generated by the stamp (γ_{elastic}) is caused by its deformation through two physical processes: 1) global deformation caused by pressing the stamp

against the substrate, and 2) local deformation dominated by factors such as the local melting of the PC film at LF, the mechanical properties of the heterobilayer, and the interfacial properties of 2D layers at LF. We will analyze the effect of these two deformation types on the interface cleaning in a later section (“elastic energy due to stamp deformation”).

2.3. Composition of the Interfacial Contaminants

We studied the structural and chemical properties of the blistered regions in PVA-contaminated BGB heterostructures through cross-sectional imaging with high-resolution transmission electron microscopy (HRTEM) and electron dispersive X-ray spectroscopy (EDS) technique. The HRTEM image in Figure 2b shows the presence of a continuous amorphous layer with a thickness of ≈ 4 nm in between hBN layers. The elemental EDS results (Figure 2c,d) indicate that the interfacial contaminants largely consist of carbon (C) atoms.

Previous TEM studies on BGB heterostructures made from conventionally exfoliated graphene have attributed the observed elemental C in the blistered regions to environmental hydrocarbons.^[38] Unlike those studies, however, the BGB sample in our TEM studies was prepared using PVA-contaminated graphene and encapsulated at high temperatures (i.e., 220 °C). This temperature should be sufficient for cleaning non-polymer contaminated vdW interfaces, as confirmed by our controlled experiments. Employing identical encapsulation conditions yielded blister-free BGB heterostructures from conventionally exfoliated graphene (Figure S3, Supporting Information). Therefore, while we do not rule out the presence of some trapped environmental hydrocarbons in the PVA-contaminated BGB samples used in our TEM studies, we attribute the observed C atoms in EDS studies primarily to PVA residues.

Surprisingly though, the EDS analysis also revealed the presence of silicon (Si) at some blistered regions (like the image in Figure 2c). We attribute this observation to residual SiO_x since the spatial profile of Si always overlapped with that of oxygen (O). The mechanism behind the incorporation of SiO_x residues is unknown and requires further investigation. By performing additional experiments (see Note S1 and Figure S4, Supporting Information), we inferred that those residues were absorbed into PVA during the exfoliation and transfer steps. These imaging studies confirmed that the polymeric residues were the dominant contaminants at the blistered regions, including those with detectable Si (e.g., notice the line intensity profiles of Si and C atoms in Figure 2d).

2.4. Polymer Interfacial Energies (γ_{pg} and γ_{pb})

The nature of PVA residue interactions with graphene and hBN determines γ_{pg} and γ_{pb} . Intuitively, we expect that weak interactions of PVA with graphene and hBN will be desirable for lowering γ_{pg} and γ_{pb} . Considering the extremely inert properties of hBN,^[42] we assumed that no strong interactions will occur between PVA residues and hBN; hence γ_{pb} is low. Unlike hBN, however, pristine graphene is known to have strong non-covalent interactions with some polymers (e.g.,

PMMA).^[30] Furthermore, the presence of structural defects in graphene could additionally drive covalent bonding to highly reactive functional groups in polymers (e.g., carbonyl groups in PMMA).^[30,43] Strong interactions (covalent or non-covalent) between polymers and graphene will result in high γ_{pg} , thus confounding the interface cleaning involving those polymers.

Our DFT calculations indicate weak non-bonding interactions between graphene and PVA molecules (See Note S3 and Figure S5, Supporting Information). The closest inter-atomic distance between PVA (hydrogen atom) and pristine graphene is 0.27 nm, which is comparable to the sum of their vdW radii. Furthermore, the shared frontier orbitals, that is, the highest occupied and lowest unoccupied molecular orbitals (HOMO and LUMO), are entirely confined to graphene, thus indicating weak interactions. Furthermore, we find that the interactions of PVA with defective graphene are driven mostly by non-covalent interactions (See Note S3 and Figure S5, Supporting Information). These DFT results suggest that PVA residues yield low γ_{pg} , a favorable factor for removing those contaminants from the vdW interfaces.

We were unable to quantitatively determine the values of γ_{pg} and γ_{pb} since those calculations are highly involved. They require independent studies to determine the precise nature of the atomic structure and composition of PVA residues during the encapsulation step.

2.5. Polymer Surface Energy (γ_p)

Polymer science studies suggest that the surface energy of polymers generally decreases with increasing temperature due to the increase of the entropic contribution to surface thermodynamic properties.^[32–34] Inspired by this phenomenon, we performed a series of temperature-dependent encapsulation experiments at elevated substrate temperatures up to 235 °C. In these experiments, we controlled for the thicknesses of t-hBN and b-hBN.

The experiments in the temperature range of 170–220 °C resulted in negligible interface cleaning. **Figure 3a** is the optical image of a representative BGB heterostructure obtained from an encapsulation at 220 °C. This image shows a highly blistered heterostructure (see Figure S6, Supporting Information, for additional optical images). **Figure 3b** is the corresponding spatial Γ_{2D} map of this heterostructure, confirming that a large portion of the heterostructure suffers from interfacial contaminants (notice regions with $\Gamma_{2D} > 20 \text{ cm}^{-1}$).

Surprisingly, we observed a sudden and remarkable enhancement of the interface cleaning by increasing the temperature above 230 °C. This observation indicates that the energy gap between γ_{elastic} and γ_{LF} (i.e., γ_p) increases by a relatively small increase in temperature (from 220 to 230 °C). To rule out an increase in γ_{elastic} as the cause, we examined the extent of the stamp elastic deformation for samples prepared at different temperatures. Our analysis showed comparable levels of stamp deformation in these samples (see Figure S7, Supporting Information).

From the analysis of the stamp deformation, we infer that the observed interface cleaning is attributable to the reduction in γ_p . The well-studied dynamic mechanical properties of

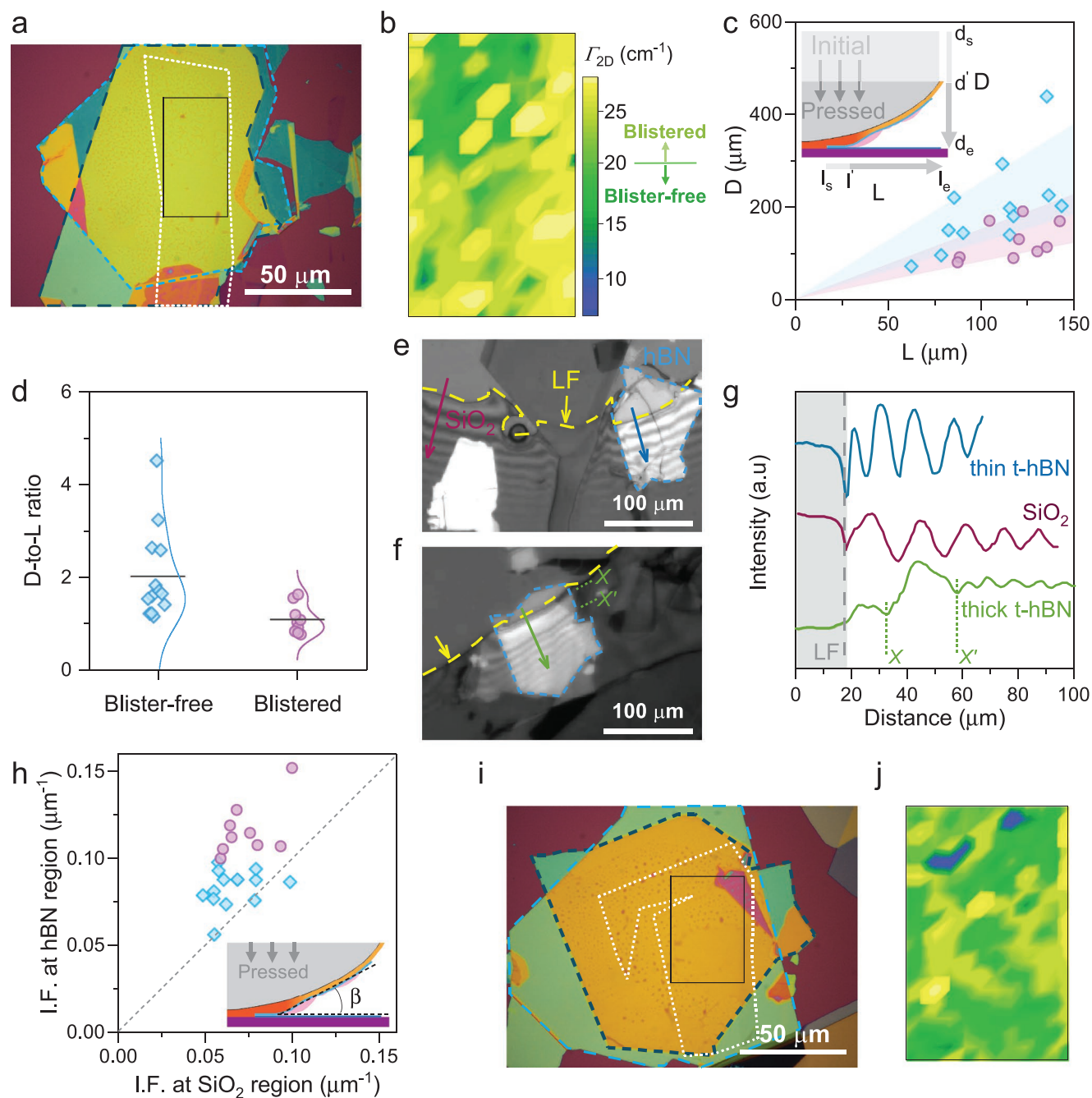


Figure 3. Experimental study of the interface cleaning problem. a) Optical image and b) corresponding Γ_{2D} map of a representative heterostructure encapsulated at 220 °C. c) The measured D plotted against the heterostructure length, L . The blue diamond (purple circle) data points are from the blister-free (blistered) heterostructures. The shadings are guides to the eye. The inset shows schematically the procedure for measuring D . d) The plot of D -to- L ratio from the same heterostructures in (c). The black line indicates the mean value. The blue (purple) curve shows the statistical distribution. e, f) Examples of optical images captured during the encapsulation experiments using thin and thick t-hBN, respectively. g) The interference fringe profiles obtained from the optical images in (e) and (f). Note the absence of fringe periodicity from the thick t-hBN in the region marked with XX' in panel (f) and (g). h) The plot of I.F. extracted at the hBN and SiO_2 regions for multiple blister-free (blue diamond) and blistered (purple circle) heterostructures. The inset shows the definition of the contact angle β . The 1:1 gray dashed line is a guide to the eye. i) Optical image, and j) corresponding Γ_{2D} map of a representative heterostructure with a 56-nm-thick t-hBN.

PVA support this interpretation. Specifically, past research has shown that PVA undergoes several different molecular relaxation events at distinct temperatures.^[31] Interestingly, one of those events occurs at around 230 °C, which coincides with the

observed temperature threshold required to achieve interface cleaning. At this temperature, pure PVA (with no moisture) experiences a sharp and dramatic crystalline relaxation (i.e., melting of its crystalline domain).^[31] This physical change of

PVA corresponds to higher entropic contributions to the surface thermodynamic properties of polymeric residues, and thus a reduction in γ_p .^[32–34]

2.6. Elastic Energy due to Stamp Deformation (γ_{elastic})

So far, we have demonstrated that a minimum substrate temperature of 230 °C is essential for mobilizing the PVA polymeric residues. Once the residues are thermally activated and become moveable, the stamp deformation must provide the required γ_{elastic} for pushing them forward at LF. Therefore, we closely examined how the global and local stamp deformations influence the outcome of the interface cleaning process.

We performed a series of encapsulation experiments at 235 °C and used the same range of t-hBN and b-hBN thicknesses (see Figure S8, Supporting Information). While most heterostructures were blister-free, these experiments also yielded a few heterostructures with noticeable amounts of interfacial blisters. We utilized these samples to understand how stamp deformations influence the removal of polymeric residues.

The elastomeric stamp in our experiments was assembled on the bottom end of a glass cantilever while its other end was affixed to a mechanical manipulator (see Figure S9, Supporting Information). As the cantilever is lowered vertically, it compresses the stamp against the substrate. As more pressure is applied, the LF continues to travel laterally along the substrate. We refer to the extent of stamp compression to complete the encapsulation of a heterostructure as the global deformation.

For each encapsulation experiment, we measure the vertical displacement as the difference in the vertical height of the stamp relative to the substrate at the start (d_s) and end (d_e) of the encapsulation process (i.e., $D = d_s - d_e$ in the inset in Figure 3c). To control for the effect of the heterostructure dimension, we measured the length of the heterostructure along the direction of LF (i.e., $L = l_s - l_e$ in the inset in Figure 3c). We then plotted the measured D against L for blistered and blister-free BGB stacks (Figure 3c).

Two observations are made from the data. For a fixed L , stamps with larger D generally produced blister-free heterostructures. This observation indicates that BGB stacks formed under a higher global stamp deformation are more likely to be blister-free. Moreover, D generally increases with L . This observation is consistent with the intuition that longer heterostructures require a more prolonged application of pressure to complete the encapsulation. Based on these observations, we used the normalized D per unit length L (i.e., D -to- L ratio) as a proxy for the global stamp deformation. In Figure 3d, we plotted this metric for the blistered and blister-free heterostructures. Given the heterostructure length, this plot can be used to determine a target D to yield blister-free heterostructures.

A closer look at the data in Figure 3d reveals an overlap between the blister-free and blistered heterostructures. This observation suggests that the global stamp deformation does not fully explain the difference in the outcome of the encapsulation experiments. We hypothesized that the local stamp deformation at LF could explain those differences. Whereas the direct measurement of the local elastic deformation is challenging, visualizing the contact angle (β) can provide

qualitative information about the local deformation (see inset in Figure 3h).

We employed the concept of the interference fringe method^[44] for extracting information about β on the same heterostructures of Figure 3c. In particular, the interference frequency (I.F.) of the fringe profile on the substrate is a function of β , where a smaller I.F. represents a smaller β (see Note S2 and Figure S10, Supporting Information). We analyzed the optical images obtained during encapsulation (like the image in Figure 3e,3f) to extract the fringe profile at SiO₂ and hBN regions (Figure 3g). By performing the fast Fourier transform of the fringe profiles, we obtained the corresponding I.F. at those regions for the blister-free and blistered heterostructures and plotted them in Figure 3h.

This analysis revealed subtle yet crucial information about the local stamp deformation. Whereas the stamps generated the same range of I.F. (and thus β) at the SiO₂ regions for both blister-free and blistered heterostructures, this analysis indicates a stark difference in β localized to the hBN regions (see Figure 3h). Interestingly, the blister-free heterostructures showed a smaller β than their blistered counterparts. The similar range of I.F. at the SiO₂ regions suggests a comparable local deformation caused by the melting of PC for the blistered and blister-free samples. Furthermore, these samples had a similar range of t-hBN thickness (see Figure S8, Supporting Information), hence ruling out the effect of the heterobilayer mechanical properties on the local stamp deformation.

The precise reason behind the observation in Figure 3h is unknown. Based on our analysis above, we attribute the observed differences in β at the hBN regions to differences in the interfacial properties between PVA-contaminated graphene and b-hBN. We suspect that it originates from the variations in the amount or the chemical composition of the interfacial contaminants (see Figure S4, Supporting Information). These results confirm that the global and local stamp deformation must be engineered to remove polymeric residues across the entire BGB heterostructures completely.

The BGB samples produced in these experiments also provide an estimate for the current yield of our interface cleaning process. About 60% of the BGB samples showed complete interface cleaning across the entire dimension of the heterostructure. This success rate can be easily improved by increasing the consistency of the elastomeric stamp production and the optimization of the stamp dimensions according to our findings for enhancing the global deformation.

We also examined how the heterobilayer thickness influences the local deformation, and hence the effective application of the driving force at LF. It is known that the rigidity of 2D materials, and thus their bending energy, increases with the number of constituent layers.^[45] Therefore, it is likely that the heterobilayers beyond a critical thickness of t-hBN will no longer fully conform to the elastomeric stamp, thereby compromising the local stamp deformation. We examined this through a series of experiments by varying the thickness of t-hBN while keeping the substrate temperature at 235 °C.

We observed a complete interface cleaning across the heterostructures only when employing t-hBN within 20–35 nm thickness range (like data points shown in Figure 3h). In contrast, the use of thicker t-hBN layers (50 nm and more)

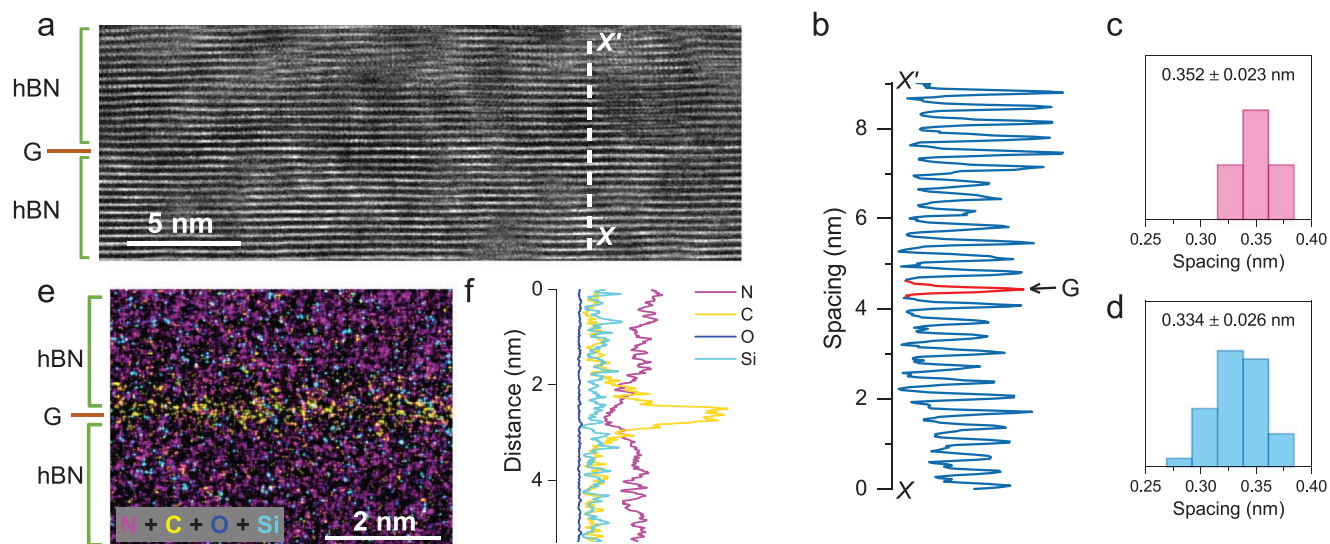


Figure 4. Evidence of atomically clean interfaces. a) A representative cross-sectional HRTEM image, showing atomically sharp interfaces of blister-free BGB heterostructures. b) Intensity profile extracted along the XX' line in panel (a). Statistical distribution of interlayer distance between c) graphene to hBN, and d) basal plane of hBN. e) Corresponding EDS map and f) averaged line intensity profile.

always resulted in blistered heterostructures (like the image in Figure 3i; see Figure S11, Supporting Information, for additional data). Figure 3j shows the corresponding spatial Γ_{2D} map of graphene, further confirming the poor interfacial quality of the resulting heterostructure.

While it is difficult to determine precisely how the t-hBN interacts with the elastomeric stamp by varying its thickness, the optical images obtained during encapsulation provided some interesting insights. Figure 3e,3f shows representative images of the encapsulations using thin and thick t-hBN flakes, respectively. These images showed a narrower and more pronounced LF line profile at the heterostructure region for thin t-hBN samples. These features are likely to be the signature of a more pronounced driving force at LF. Moreover, thin t-hBN samples showed periodic interference fringes along the entire length of the hBN. Thick t-hBN samples, however, lacked this feature (see Figure 3g). We suspect that the disruption of the periodic fringes in samples with thick t-hBN signifies a degradation in their full mechanical compliance to the stamp. Therefore, the thickness of t-hBN provides another degree of freedom for engineering the stamp to produce blister-free BGB heterostructures.

Last, let us comment on the effect of LF speed. In our experiments, the interface cleaning showed moderate sensitivity to the LF speed. A relatively broad range of LF speed ($2\text{--}20\ \mu\text{m s}^{-1}$) yielded complete interface cleaning across the heterostructures. In this optimal range, we generally picked a speed that provided a more controlled manipulation of the LF during the layered assembly. The preferred LF speed was about 10 and $4\ \mu\text{m s}^{-1}$ for the manual and automated (QPress) layered assembly setups, respectively.

2.7. Evidence of Atomically Clean Interfaces

We examined the structural properties of the clean BGB heterostructures produced from PVA-contaminated graphene

using cross-sectional HRTEM imaging. A representative HRTEM image obtained from a clean BGB sample is shown in Figure 4a, indicating well-defined and abrupt interfaces between graphene and hBN. By analyzing the intensity profiles extracted from the HRTEM images (like the plot in Figure 4b), we determined the graphene-hBN inter-distance to be $0.352\pm 0.023\ \text{nm}$ (Figure 4c). Remarkably, this spacing, within experimental accuracy, is similar to the extracted basal plane separation in bulk hBN ($0.334\pm 0.026\ \text{nm}$, Figure 4d), thus confirming atomically sharp interfaces between graphene and hBN. These findings agree with the elemental characterization of these heterointerfaces (see Figure 4e,f), which revealed no detectable Si or O atoms.

2.8. Electronic Transport Properties

The carrier transport properties of graphene can provide strong evidence for the structural quality of the BGB heterostructures. To study the quality of the 2D electronic system in graphene, we fabricated large square-shaped devices with electrical edge contacts on clean BGB heterostructures (like that shown in Figure 5a). This device structure is favorable for transport studies as it can provide an unambiguous signature for the ballistic transport of charge carriers.^[14–16] The spatial Γ_{2D} mapping was employed to confirm the cleanliness of the heterointerfaces across the BGB stack (Figure 5b). In Figure 5c, we show the optical image of the resulting square-shaped device with an edge length of $12\ \mu\text{m}$ and the four-point measurement configuration used for studying the carrier transport. The carrier density (n) in graphene was modulated by applying a voltage to the global back gate (see Experimental Section for device fabrication and measurements).

Analysis of the electrical measurement results confirmed the high quality of the electronic system in graphene. Figure 5d shows the four-terminal resistivity of the device measured at

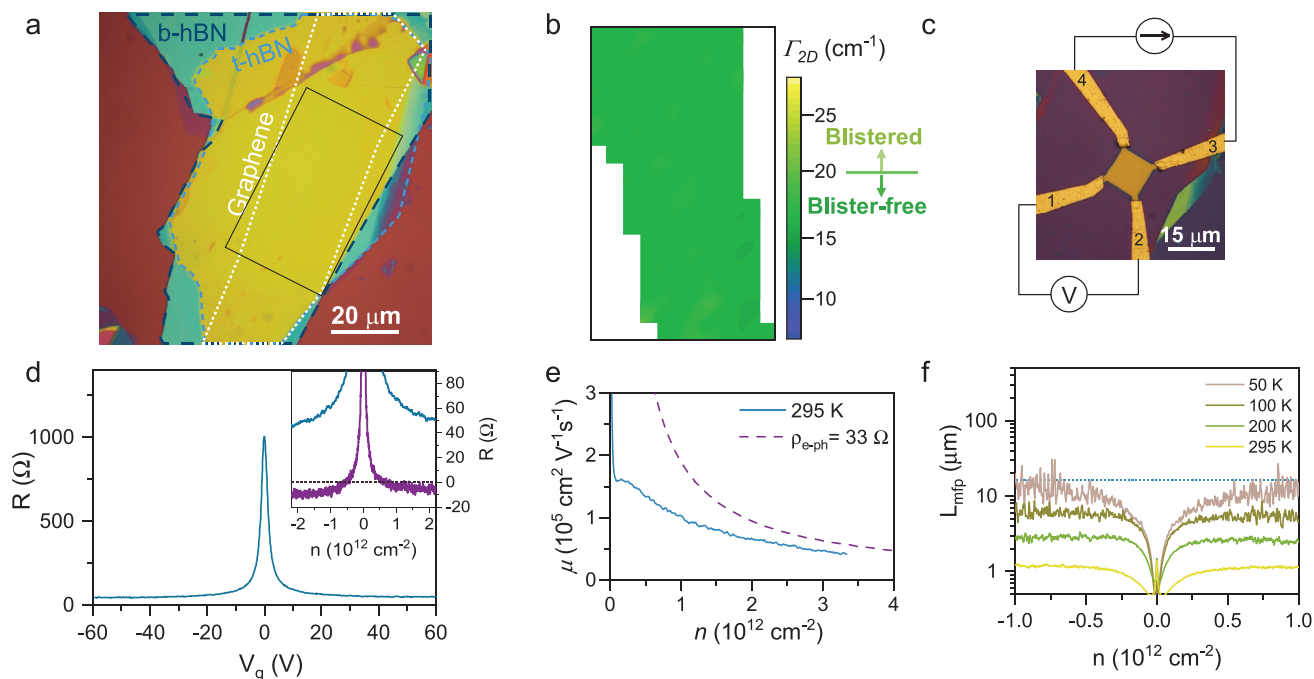


Figure 5. Electronic transport properties. a) Optical image of a BGB heterostructure used for device fabrication. b) Corresponding spatial Γ_{2D} map obtained from the region marked with a solid rectangle. c) Optical image of a square-shaped device and the illustration of the electrical measurement configuration. d) Room-temperature measurement of graphene sheet resistance. The inset in (d) shows the negative resistance measured at 1.5 K, indicating ballistic transport across the device. e) Room-temperature mobility as a function of carrier density, n . The dashed line shows the theoretical limit of phonon scattering at room temperature. f) L_{mfp} plotted at different temperatures. Below 50 K, L_{mfp} approaches the device dimension (the blue dashed line).

room temperature as a function of the back-gate voltage (V_g). From the data, the charge neutrality point occurs at $V_g = 0.2$ V, indicating a highly intrinsic sample. Using the Drude model of conductivity ($\sigma = en\mu$), we calculated the mobility (μ) at room temperature, as shown in Figure 5e. These results show that the room-temperature performance of this graphene device matches state-of-the-art counterparts prepared using the dry transfer methods.

At low temperatures, the four-point resistivity was measured and used to calculate the mean free path ($L_{mfp} = (\hbar/2e^2)\sigma/k_F$), where k_F is the Fermi wavevector. As shown in Figure 5f, L_{mfp} increased by reducing the temperature and approached the device size at 50 K. The device resistance began to show negative resistance values below 50 K, making the calculation of L_{mfp} unreliable. Remarkably, the observation of a negative resistance at the base temperature of 1.5 K (inset in Figure 5d) indicates that electron and hole carriers travel ballistically (i.e., with no scattering) across the diagonal of the device (e.g., from probe 3 to 1 in Figure 5c). This corresponds to a minimum L_{mfp} of 17 μm , which gives lower bound mobility of ≈ 1000000 at n of $\approx 2 \times 10^{12} \text{ cm}^{-2}$. Collectively, the excellent electronic properties of graphene reported here further support the high structural quality of the BGB samples produced in our experiments. These results are consistent among graphene devices fabricated on different BGB heterostructures (see Note S4 and Figures S12 and S13, Supporting Information), indicating the high uniformity of our approach in producing high-quality 2D electronic systems in graphene.

3. Discussion

The study presented here introduces and experimentally verifies a systematic framework for removing polymeric contaminants from the vdW interfaces. This framework allows us to establish the mechanisms behind the interface cleaning of polymer-contaminated interfaces, resulting in a fabrication approach that can systematically produce large-area blister-free BGB heterostructures. By applying this framework to PVA-contaminated graphene, we demonstrate record large-area BGB heterostructures (up to 7500 μm^2 , see Figure S2, Supporting Information) with atomically clean interfaces. The resulting heterostructures show excellent electronic properties on par with state-of-the-art counterparts prepared using the conventional methods.

The blister-free heterostructures obtained from PVA-contaminated graphene in our experiments have over 10 times larger area than the previous champion PMMA-contaminated heterostructure reported in ref. [16]. The maximum area of these blister-free heterostructures does not represent a fundamental limit of our interface cleaning concept. This is supported by the fact that the interfacial contaminants were consistently pushed away to the borders of these heterostructures (e.g., see line blisters in Figure 1h). The dimension of the heterostructures in our experiments was constrained by the available size of hBN flakes. Hence, an important future research direction for scaling up the dimensions of the BGB heterostructures is the production of large-area hBN layers with high structural quality on par with those obtained from the mechanical exfoliation.

Our results establish that the chemical and dynamic mechanical properties of polymeric residues determine the outcome of the cleaning process. The low chemical reactivity of PVA yields non-bonding interactions with graphene, and hence low γ_{pg} . This property of PVA contrasts with that of PMMA, which is known to bond covalently to defective graphene and even has strong non-covalent interactions with pristine graphene (i.e., high γ_{pg}).^[30,43] These properties of PMMA, predicted by DFT calculations, could be one of the limiting factors behind the previously observed incomplete interface cleaning in PMMA-contaminated BGB heterostructures.^[16,28]

Our experiments also revealed a sharp transition in the temperature-dependent cleaning behavior, which coincides with a distinct molecular relaxation event in PVA. By increasing the entropic contribution to surface thermodynamic properties, this property of the polymer decreases surface energy (γ_p), thereby increasing its surface mobility. This observation, combined with DFT calculations, provides critical guidelines for choosing appropriate polymers for preparing and handling 2D layers used in constructing vdW heterostructures.

Our results show that increasing the extent of stamp deformation yields a more effective removal of mobile polymeric residues. Based on these findings, systematic engineering of the stamp, in terms of shape and dimensions, is an important research direction to maximize the global elastic deformation. Moreover, our approach for analyzing the local elastic deformation using the interference fringe method points to new strategies for studying the mechanics of encapsulation and developing predictive capabilities in automated layered assembly machines.

Our study establishes the excellent electronic properties of BGB heterostructures obtained from the PVA-contaminated graphene. These BGB heterostructures may be helpful in many technological applications, from THz electronics^[46] to single-photon sensing.^[9] Furthermore, it may be possible to extend our findings for fabricating other vdW heterostructures (see the prototype hBN/graphene/WS₂/hBN heterostructures in Figure S14, Supporting Information). These results, although preliminary, are encouraging, indicating the prospects of our approach for fabricating more complex heterostructures. However, the feasibility of PVA-contaminated graphene for realizing moiré superlattices with small twist angles will be highly challenging. In particular, the required high temperature for mobilizing PVA could promote the relaxation of the moiré superlattices.^[47,48] This limitation highlights the need for an alternative polymer in handling 2D layers that can be mobilized at significantly lower temperatures.

These results have important implications for advancing the knowledge of 2D materials processing. While PVA has been a polymer of interest for handling 2D materials due to its water solubility, biocompatibility, and favorable mechanical properties,^[25,49–52] little is done to study the cleaning of PVA-contaminated 2D layers, including graphene. Our study takes an important step to advance this knowledge. Furthermore, our study demonstrates clean heterostructures with record large dimensions, thereby establishing that PVA contamination of graphene is not a fundamental barrier. Critically, our DFT calculations also indicate that no covalent bond would form between PVA and defective graphene. Considering the more defective

nature of CVD films than their exfoliated counterparts, an exciting future research direction is to investigate the applicability of our approach for constructing clean heterostructures from CVD graphene. This would be a crucial step for driving vdW heterostructures toward technological applications.

4. Experimental Section

Preparation of the Stamp Assembly: The elastomeric stamp consisted of a thin layer of poly (bisphenol A carbonate) (PC) film (a few μm) on a hemispherical polydimethylsiloxane (PDMS) base. To construct the hemispherical shape, the PDMS was drop-cast onto a glass slide and cured at 150 °C for 10 min. The PC film was prepared following a similar procedure in ref. [53]. The PC film was then cut into 5 × 5 mm² blocks using a razor blade and mounted onto PDMS. The PC/PDMS/glass stamp assembly was baked at 150 °C for 10 min to complete the construction.

Preparation of Graphene and hBN flakes: In all experiments, monolayer graphene was prepared using the PAGE method.^[25] The graphene exfoliation used silicon substrates covered with 285 nm SiO₂. Prior to exfoliation, these substrates were coated with a sub-10-nm PVA film. After exfoliation, candidate graphene flakes were identified using optical microscopy, and their monolayer thickness was confirmed using Raman spectroscopy. In all experiments, the hBN flakes were prepared following a similar procedure in ref. [54].

Construction of BGB Heterostructures: The stamp assembly was first used to pick up a t-hBN flake at 150 °C, which was around the glass transition temperature of the PC.^[55,56] Next, the t-hBN flake on the stamp was brought into contact with a target monolayer graphene flake at T ≈ 80 °C, which was below the boiling temperature of water. While the stamp was in contact with monolayer graphene, a drop of deionized water was locally injected to dissolve the PVA layer underneath graphene, resulting in the release of graphene from the substrate. The stamp assembly containing the t-hBN/graphene heterobilayer was then placed in a deionized water bath for one hour to remove residual PVA from the graphene surface further. The stamp assembly was stored in a vacuum desiccator at room temperature before its use for completing the construction of BGB heterostructures.

In the experiments, the heterobilayer was intentionally placed away from the lowest region of the hemispherical stamp. This design ensured that the initial LF was located away from the target b-hBN substrate, thus providing improved control to perform encapsulation. Encapsulation at elevated temperatures (in the range of 170 to 235 °C) completed the construction of BGB heterostructures.

Development of the Interface Cleaning Framework: An iterative workflow using a manual assembly setup was initially designed. The implementation of the workflow involved over 140 encapsulation experiments, which provided critical insights into various factors that influence the interface cleaning process. Utilizing those results, the simplified picture of the interface cleaning was conceived, which hypothesizes the physical processes involved in removing the polymeric residues during the encapsulation step.

To reveal the interface cleaning mechanisms, additional encapsulation experiments (over 100) were performed using the Quantum Materials Press (QPress) facility developed at Brookhaven National Laboratory,^[57] which is a set of integrated tools meant to streamline the exfoliation and handling of ultrathin and 2D materials. The 2D material transfer module of QPress, or “Stacker,” is a custom-built automated precision robot specialized for stacking vdW heterostructures. It permits precise manipulation of the stamp assembly using a hexapod with six degrees of freedom (i.e., complete translation and orientational control), and positioning of the sample with three degrees of freedom (lateral position and in-plane orientation). The system records parameters during experimental execution (motor positions, substrate temperature, etc.), and records video of the experiment (e.g., moving contact line) through an integrated optical microscope. This setup enables reproducible motion, systematic studies, and quantitative analysis

TEM Sample Preparation: TEM lamellas were prepared in the Thermo Fisher Helios G5 UX dual-beam FIB tool utilizing the in situ lift-out sample preparation technique. All TEM samples were thinned with a Ga⁺ ion beam using progressively lower beam voltages ending with 2 keV.

TEM and STEM X-ray micro analysis were conducted in a Thermo Fisher Talos 200X STEM/TEM at 200 keV and equipped with the Super-X EDS Detection System.

Fabrication and Electrical Measurements of BGB Devices: The patterning of the device mesa involved a combination of electron-beam lithography and reactive ion etching. The electrical contact to graphene was then formed using the edge contact method.^[14] The metal electrode consists of an electron-beam evaporated stack of Cr/Pd/Au (5/30/30 nm).

The transport measurements of graphene devices were made employing low-current, low-frequency lock-in techniques. The temperature-dependent measurements were made in TeslatronPT (a cryo-free superconducting magnet system).

Supporting Information

Supporting Information is available from the Wiley Online Library or from the author.

Acknowledgements

The authors acknowledge partial financial support from NSF (grants EECS-1940764). K.W. and T.T. acknowledge support from the Elemental Strategy Initiative conducted by the MEXT, Japan (Grant Number JPMXP0112101001) and JSPS KAKENHI (Grant Numbers 19H05790, 20H00354 and 21H05233). This work was performed in part at the ASRC NanoFabrication Facility of CUNY in New York. This research used resources of the Center for Functional Nanomaterials (CFN), which is a U.S. Department of Energy Office of Science User Facility, at Brookhaven National Laboratory under Contract No. DE-SC0012704. D.S. acknowledges Prof. J. Uichanco at the University of Michigan Ann Arbor and Dr. C. Black at the Center for Functional Nanomaterials at BNL for helpful discussions.

Conflict of Interest

The authors declare no conflict of interest.

Author Contributions

Z.H. and D.S. conceived and designed the experiments. Z.H., E.C., and D.S. performed the experiments and contributed to the data analysis. S.P. and K.G.Y. contributed to the experiments using QPress. K.K. performed the TEM studies. Q.W. performed the DFT calculations. K.W. and T.T. prepared the hBN material. The manuscript was written with input from all authors.

Data Availability Statement

The data that support the findings of this study are available in the supplementary material of this article.

Keywords

graphene, heterostructures, interface cleaning, transport

Received: February 25, 2022
Published online: April 7, 2022

- [1] Y. Kim, A. C. Balram, T. Taniguchi, K. Watanabe, J. K. Jain, J. H. Smet, *Nat. Phys.* **2019**, *15*, 154.
- [2] K. Komatsu, Y. Morita, E. Watanabe, D. Tsuya, K. Watanabe, T. Taniguchi, S. Moriyama, *Sci. Adv.* **2018**, *4*, eaaq0194.
- [3] L. Bretheau, J. I.-J. Wang, R. Pisoni, K. Watanabe, T. Taniguchi, P. Jarillo-Herrero, *Nat. Phys.* **2017**, *13*, 756.
- [4] F. Amet, C. T. Ke, I. V. Borzenets, J. Wang, K. Watanabe, T. Taniguchi, R. S. Deacon, M. Yamamoto, Y. Bomze, S. Tarucha, G. Finkelstein, *Science* **2016**, *352*, 966.
- [5] G.-H. Lee, K.-F. Huang, D. K. Efetov, D. S. Wei, S. Hart, T. Taniguchi, K. Watanabe, A. Yacoby, P. Kim, *Nat. Phys.* **2017**, *13*, 693.
- [6] M. Ben Shalom, M. J. Zhu, V. I. Fal'ko, A. Mishchenko, A. V. Kretinin, K. S. Novoselov, C. R. Woods, K. Watanabe, T. Taniguchi, A. K. Geim, J. R. Prance, *Nat. Phys.* **2016**, *12*, 318.
- [7] J. I. Wang, D. Rodan-Legrain, L. Bretheau, D. L. Campbell, B. Kannan, D. Kim, M. Kjaergaard, P. Krantz, G. O. Samach, F. Yan, J. L. Yoder, *Nat. Nanotechnol.* **2019**, *14*, 120.
- [8] G.-H. Lee, D. K. Efetov, W. Jung, L. Ranzani, E. D. Walsh, T. A. Ohki, T. Taniguchi, K. Watanabe, P. Kim, D. Englund, K. C. Fong, *Nature* **2020**, *586*, 42.
- [9] E. D. Walsh, W. Jung, G.-H. Lee, D. K. Efetov, B.-I. Wu, K.-F. Huang, T. A. Ohki, T. Taniguchi, K. Watanabe, P. Kim, D. Englund, K. C. Fong, *Science* **2021**, *372*, 409.
- [10] C. R. Dean, A. F. Young, I. Meric, C. Lee, L. Wang, S. Sorgenfrei, K. Watanabe, T. Taniguchi, P. Kim, K. L. Shepard, J. Hone, *Nat. Nanotechnol.* **2010**, *5*, 722.
- [11] X. Hong, K. Zou, J. Zhu, *Phys. Rev. B* **2009**, *80*, 241415.
- [12] E. H. Hwang, S. Das Sarma, *Phys. Rev. B* **2008**, *77*, 195412.
- [13] M. Monteverde, C. Ojeda-Aristizabal, R. Weil, K. Bennaceur, M. Ferrier, S. Guéron, C. Glattli, H. Bouchiat, J. N. Fuchs, D. L. Maslov, *Phys. Rev. Lett.* **2010**, *104*, 126801.
- [14] L. Wang, I. Meric, P. Y. Huang, Q. Gao, Y. Gao, H. Tran, T. Taniguchi, K. Watanabe, L. M. Campos, D. A. Muller, J. Guo, P. Kim, J. Hone, K. L. Shepard, C. R. Dean, *Science* **2013**, *342*, 614.
- [15] A. S. Mayorov, R. V. Gorbachev, S. V. Morozov, L. Britnell, R. Jalil, L. A. Ponomarenko, P. Blake, K. S. Novoselov, K. Watanabe, T. Taniguchi, A. K. Geim, *Nano Lett.* **2011**, *11*, 2396.
- [16] D. G. Purdie, N. M. Pugno, T. Taniguchi, K. Watanabe, A. C. Ferrari, A. Lombardo, *Nat. Commun.* **2018**, *9*, 5387.
- [17] S. B. Desai, S. R. Madhvapathy, M. Amani, D. Kiriya, M. Hettick, M. Tosun, Y. Zhou, M. Dubey, J. W. Ager, D. Chrzan, A. Javey, *Adv. Mater.* **2016**, *28*, 4053.
- [18] M. Velický, G. E. Donnelly, W. R. Hendren, S. McFarland, D. Scullion, W. J. I. Debenetti, G. C. Correa, Y. Han, A. J. Wain, M. A. Hines, D. A. Muller, K. S. Novoselov, H. D. Abruña, R. M. Bowman, E. J. G. Santos, F. Huang, *ACS Nano* **2018**, *12*, 10463.
- [19] A. Alharbi, Z. Huang, T. Taniguchi, K. Watanabe, D. Shahrjerdi, *IEEE Electron Device Lett.* **2018**, *40*, 135.
- [20] K. Kang, K.-H. Lee, Y. Han, H. Gao, S. Xie, D. A. Muller, J. Park, *Nature* **2017**, *550*, 229.
- [21] J. Kim, H. Park, J. B. Hannon, S. W. Bedell, K. Fogel, D. K. Sadana, C. Dimitrakopoulos, *Science* **2013**, *342*, 833.
- [22] F. Liu, W. Wu, Y. Bai, S. H. Chae, Q. Li, J. Wang, J. Hone, X.-Y. Zhu, *Science* **2020**, *367*, 903.
- [23] J.-Y. Moon, M. Kim, S.-I. Kim, S. Xu, J.-H. Choi, D. Whang, K. Watanabe, T. Taniguchi, D. S. Park, J. Seo, S. H. Cho, S.-K. Son, J.-H. Lee, *Sci. Adv.* **2020**, *6*, eabc6601.
- [24] J. Shim, S.-H. Bae, W. Kong, D. Lee, K. Qiao, D. Nezich, Y. J. Park, R. Zhao, S. Sundaram, X. Li, H. Yeon, C. Choi, H. Kum, R. Yue, G. Zhou, Y. Ou, K. Lee, J. Moodera, X. Zhao, J.-H. Ahn, C. Hinkle, A. Ougazzaden, J. Kim, *Science* **2018**, *362*, 665.
- [25] Z. Huang, A. Alharbi, W. Mayer, E. Cuniberto, T. Taniguchi, K. Watanabe, J. Shabani, D. Shahrjerdi, *Nat. Commun.* **2020**, *11*, 3029.

- [26] L. Lin, J. Zhang, H. Su, J. Li, L. Sun, Z. Wang, F. Xu, C. Liu, S. Lopatin, Y. Zhu, K. Jia, *Nat. Commun.* **2019**, *10*, 1912.
- [27] M. Wang, M. Huang, D. Luo, Y. Li, M. Choe, W. K. Seong, M. Kim, S. Jin, M. Wang, S. Chatterjee, Y. Kwon, Z. Lee, R. S. Ruoff, *Nature* **2021**, *596*, 519.
- [28] D. De Fazio, D. G. Purdie, A. K. Ott, P. Braeuninger-Weimer, T. Khodkov, S. Goossens, T. Taniguchi, K. Watanabe, P. Livreri, F. H. L. Koppens, S. Hofmann, I. Goykhman, A. C. Ferrari, A. Lombardo, *ACS Nano* **2019**, *13*, 8926.
- [29] J. W. Suk, A. Kitt, C. W. Magnuson, Y. Hao, S. Ahmed, J. An, A. K. Swan, B. B. Goldberg, R. S. Ruoff, *ACS Nano* **2011**, *5*, 6916.
- [30] W. S. Leong, H. Wang, J. Yeo, F. J. Martin-Martinez, A. Zubair, P.-C. Shen, Y. Mao, T. Palacios, M. J. Buehler, J.-Y. Hong, J. Kong, *Nat. Commun.* **2019**, *10*, 867.
- [31] J.-S. Park, J.-W. Park, E. Ruckenstein, *J. Appl. Polym. Sci.* **2001**, *82*, 1816.
- [32] D. N. Theodorou, *Macromolecules* **1989**, *22*, 4578.
- [33] D. Kwok, et al., *Polym. Eng. Sci.* **1998**, *38*, 757.
- [34] R.-J. Roe, *J. Phys. Chem.* **1968**, *72*, 2013.
- [35] D. A. Sanchez, Z. Dai, P. Wang, A. Cantu-Chavez, C. J. Brennan, R. Huang, N. Lu, *Proc. Natl. Acad. Sci. U. S. A.* **2018**, *115*, 7884.
- [36] B. H. Tan, J. Zhang, J. Jin, C. H. Ooi, Y. He, R. Zhou, K. Ostrikov, N.-T. Nguyen, H. An, *Nano Lett.* **2020**, *20*, 3478.
- [37] E. Khestanova, F. Guinea, L. Fumagalli, A. K. Geim, I. V. Grigorieva, *Nat. Commun.* **2016**, *7*, 12587.
- [38] S. J. Haigh, A. Gholinia, R. Jalil, S. Romani, L. Britnell, D. C. Elias, K. S. Novoselov, L. A. Ponomarenko, A. K. Geim, R. Gorbachev, *Nat. Mater.* **2012**, *11*, 764.
- [39] F. Pizzocchero, L. Gammelgaard, B. S. Jessen, J. M. Caridad, L. Wang, J. Hone, P. Bøggild, T. J. Booth, *Nat. Commun.* **2016**, *7*, 11894.
- [40] A. C. Ferrari, D. M. Basko, *Nat. Nanotechnol.* **2013**, *8*, 235.
- [41] C. Neumann, S. Reichardt, P. Venezuela, M. Drögeler, L. Banszerus, M. Schmitz, K. Watanabe, T. Taniguchi, F. Mauri, B. Beschoten, S. V. Rotkin, C. Stampfer, *Nat. Commun.* **2015**, *6*, 8429.
- [42] Y. Lei, S. Pakhira, K. Fujisawa, H. Liu, C. Guerrero-Bermea, T. Zhang, A. Dasgupta, L. M. Martinez, S. Rao Singamaneni, K. Wang, J. Shallenberger, A. L. Elias, R. Cruz-Silva, M. Endo, J. L. Mendoza-Cortes, M. Terrones, *Mater. Today* **2021**, *51*, 108.
- [43] Y.-C. Lin, C.-C. Lu, C.-H. Yeh, C. Jin, K. Suenaga, P.-W. Chiu, *Nano Lett.* **2012**, *12*, 414.
- [44] H. Li, K. Tanaka, K. Iwamoto, *Langmuir* **2020**, *36*, 14892.
- [45] E. Han, J. Yu, E. Annevelink, J. Son, D. A. Kang, K. Watanabe, T. Taniguchi, E. Ertekin, P. Y. Huang, A. M. Van Der Zande, *Nat. Mater.* **2020**, *19*, 305.
- [46] L. Viti, D. G. Purdie, A. Lombardo, A. C. Ferrari, M. S. Vitiello, *Nano Lett.* **2020**, *20*, 3169.
- [47] Y. Cao, V. Fatemi, S. Fang, K. Watanabe, T. Taniguchi, E. Kaxiras, P. Jarillo-Herrero, *Nature* **2018**, *556*, 43.
- [48] A. Kerelsky, L. J. Mcgilly, D. M. Kennes, L. Xian, M. Yankowitz, S. Chen, K. Watanabe, T. Taniguchi, J. Hone, C. Dean, A. Rubio, A. N. Pasupathy, *Nature* **2019**, *572*, 95.
- [49] Z. Li, Y. Lv, L. Ren, J. Li, L. Kong, Y. Zeng, Q. Tao, R. Wu, H. Ma, B. Zhao, D. Wang, *Nat. Commun.* **2020**, *11*, 1151.
- [50] I. Meric, C. R. Dean, A. F. Young, N. Baklitskaya, N. J. Tremblay, C. Nuckolls, P. Kim, K. L. Shepard, *Nano Lett.* **2011**, *11*, 1093.
- [51] F. Yang, J. Li, Y. Long, Z. Zhang, L. Wang, J. Sui, Y. Dong, Y. Wang, R. Taylor, D. Ni, W. Cai, P. Wang, T. Hacker, X. Wang, *Science* **2021**, *373*, 337.
- [52] S. Larentis, J. R. Tolsma, B. Fallahzad, D. C. Dillen, K. Kim, A. H. Macdonald, E. Tutuc, *Nano Lett.* **2014**, *14*, 2039.
- [53] P. J. Zomer, M. H. D. Guimarães, J. C. Brant, N. Tombros, B. J. Van Wees, *Appl. Phys. Lett.* **2014**, *105*, 013101.
- [54] A. G. F. Garcia, M. Neumann, F. Amet, J. R. Williams, K. Watanabe, T. Taniguchi, D. Goldhaber-Gordon, *Nano Lett.* **2012**, *12*, 4449.
- [55] N. Sharnim, Y. P. Koh, S. L. Simon, G. B. McKenna, *J. Polym. Sci., Part B: Polym. Phys.* **2014**, *52*, 1462.
- [56] H. Yin, S. Napolitano, A. Schönhals, *Macromolecules* **2012**, *45*, 1652.
- [57] Quantum Materials Press, <https://www.bnl.gov/qpress/> (accessed: October 2021).